ACS NANO

Cite This: *ACS Nano* 2018, 12, 6926−6937

www.acsnano.org

ARTICLE

Dynamics of Cellulose Nanocrystal Alignment during 3D Printing

Michael K. Hausmann,[†,‡] Patrick A. Rühs,[*,†] Gilberto Siqueira,[*,†,‡] Jörg Läuger,[§] Rafael Libanori,[†] Tanja Zimmermann,[‡] and André R. Studart[*,†]

[†]Complex Materials, Department of Materials, ETH Zürich, 8093 Zürich, Switzerland

[‡]Applied Wood Materials Laboratory, Empa, Swiss Federal Laboratories for Materials Science and Technology, 8600 Dübendorf, Switzerland

[§]Anton Paar Germany GmbH, Helmuth-Hirth-Strasse 6, D-73760 Ostfildern, Germany

Supporting Information

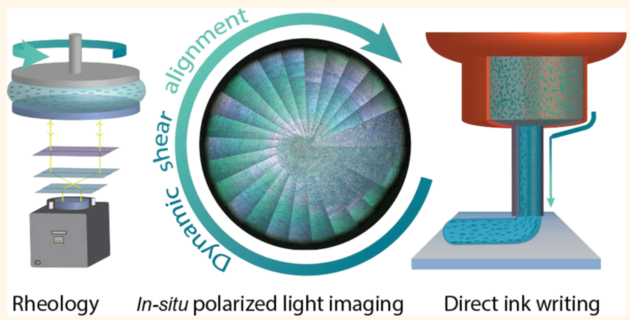

ABSTRACT: **The alignment of anisotropic particles during ink deposition directly affects the microstructure and properties of materials manufactured by extrusion-based 3D printing. Although particle alignment in diluted suspensions is well described by analytical and numerical models, the dynamics of particle orientation in the highly concentrated inks typically used for printing *via* direct ink writing (DIW) remains poorly understood. Using cellulose nanocrystals (CNCs) as model building blocks of increasing technological relevance, we study the dynamics of particle alignment under the shear stresses applied to concentrated inks during DIW. With the help of *in situ* polarization rheology, we find that the time period needed for particle alignment scales inversely with the applied shear rate and directly with the particle concentration. Such dependences can be quantitatively described by a simple scaling relation and qualitatively interpreted in terms of steric and hydrodynamic interactions between particles at high shear rates and particle concentrations. Our understanding of the alignment dynamics is then utilized to estimate the effect of shear stresses on the orientation of particles during the printing process. Finally, proof-of-concept experiments show that the combination of shear and extensional flow in 3D printing nozzles of different geometries provides an effective means to tune the orientation of CNCs from fully aligned to core−shell architectures. These findings offer powerful quantitative guidelines for the digital manufacturing of composite materials with programmed particle orientations and properties.**

KEYWORDS: *cellulose nanocrystals, rheology, polarized light, alignment, 3D printing, birefringence, shear stress, direct ink writing*

Three-dimensional (3D) printing is an enticing manufacturing technology because it enables the fabrication of materials with intricate macroscopic shapes and controlled microstructures and properties.[1−6] An effective way to locally control the structure and functionalities of composite materials is to align anisotropic particles in deliberate orientations to reach site-specific properties. Controlled particle orientation during 3D printing has been achieved using for example magnetic fields,[7−10] shear stresses,[9,11−13] or acoustic waves[14] in extrusion-based and stereolithographic processes. Among the anisotropic particles used thus far in 3D-printed composites, cellulose is of particular relevance, as it is a sustainable resource that combines biocompatibility with interesting mechanical and optical properties.[13,15−24] Cellulose can be found as anisotropic reinforcing material in the form of small, stiff nanocrystals (CNCs) or long and flexible fibrils (CNFs).

The alignment of CNCs and other anisotropic particles during 3D printing holds enormous potential since it allows one to mimic the design principles underlying the exquisite multiscale architectures of biological materials such as wood, plant stems, bone, and mollusk shells.[2] Alignment of such particles by shear stresses is a particularly interesting approach because shear-inducing flow is intrinsically present in extrusion-based 3D printing processes.[1,2,11−13,25] While it is well known that anisotropic particles align during extrusion, only a few studies have attempted to quantify the degree and dynamics of alignment in particle-filled inks.[9,11,13] Prior to alignment, anisotropic particles tend to form percolating networks that give rise to a finite yield stress, below which the ink does not flow. Particle alignment above the yield stress

Received: March 29, 2018
Accepted: July 5, 2018
Published: July 5, 2018

DOI: 10.1021/acsnano.8b02366
ACS Nano 2018, 12, 6926−6937

Scheme 1. Alignment of cellulose nanocrystal particles during shearing in a direct ink writing process (left) and in an *in situ* polarization rheological setup (right). Left: Schematic of a 3D printing process with (a1) randomly organized cellulose nanocrystals in the cartridge, (b1) shear-induced alignment during extrusion through the nozzle, and (c1) the final oriented extruded segment. During extrusion, the CNC is aligned due to a velocity profile that arises from the shear stress imposed on the suspension (TEM image with scale bar 100 nm). Right: Alignment of CNCs under shearing conditions visualized through *in situ* polarization rheology using a parallel plate geometry. The polarized light imaging system is integrated in the rheometer setup to enable investigation of the effect of shear rate and time on the CNC orientation process (a2, b2, and c2).[47]

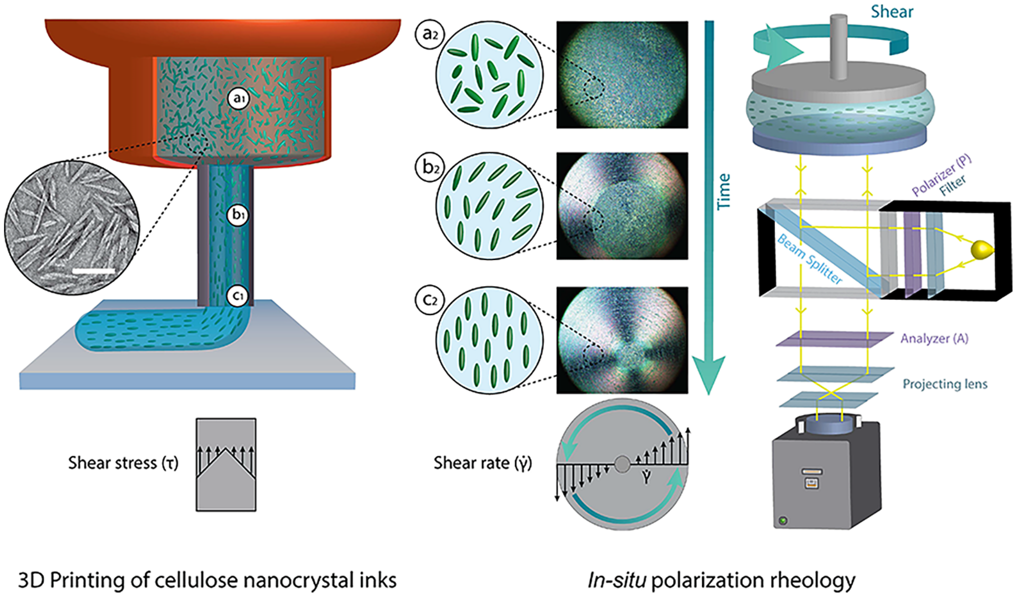

results in a strong shear-thinning response of the ink and thus a pronounced parabolic velocity flow profile within the nozzle.[26−28] Understanding the dynamics of particle alignment and the flow behavior of the resulting non-Newtonian fluids is therefore required to design inks, nozzles, and extrusion conditions to 3D print composites with programmed local structures and properties.

The alignment dynamics determine whether anisotropic particles will be oriented by the flow within the residence time in the nozzle. Particle alignment can be induced by both shear and extensional flow.[29] For the well-studied case of pure shear flow, particles move following orbital trajectories, known as Jeffery orbitals.[30,31] The time period (t) that an anisotropic particle needs to undergo a full rotation within a Jeffery orbital scales with the inverse of the applied shear rate ($\dot{\gamma}$): $t \sim 1/\dot{\gamma}$.[32−34] When suspended in non-Newtonian fluids, particles show Jeffery orbitals that drift over time until an equilibrium orientation is reached.[30,31] Because they do not take into account steric, hydrodynamic, and contact interactions between particles, such theoretical analyses are usually not sufficient to describe the alignment of anisotropic particles at high volume fractions. Recent work has shown that contact interactions play a key role in the microstructures and properties of highly concentrated suspensions of short fiber bundles used for composite fabrication.[35,36] Experimental validation of these models requires the use of analytical tools that can follow particle orientation during flow. Several experimental methods have been employed for that purpose, including rheology, neutron and X-ray scattering techniques, and optical microscopy.[37−45]

Another attractive tool for the experimental study of the flow-induced alignment of optically anisotropic materials is the polarized light imaging technique. In this approach, particle orientation is tracked during flow by color changes resulting from the varying angle between the particle axis and the orientation of the polarizer/analyzer. Polarized light imaging has been extensively used to investigate the effect of flow on the structure of liquid crystal polymers under shear flow.[33,46−50] The different nematic, smectic, and cholesteric phases that result from the self-assembly of liquid crystals were found to be directly affected by flow. When subjected to shear flow, for example, such phases transform into stripes with herringbone patterns, whose thickness decreases with the applied shear.[51] Such flow-induced textures further expand the rich phase behavior of such self-assembling systems.

While theoretical models have been put forward to describe the flow-induced orientation in particle suspensions and studies on liquid crystal polymers have provided important insights into the phase behavior of self-assembling systems under flow, experimental investigations on the dynamics of alignment of self-assembling anisotropic particles in highly concentrated suspensions of relevance for 3D printing remain scarce.[9,44] The self-assembly of Brownian anisotropic particles in concentrated printable inks promotes the formation of liquid crystalline phases prior to the extrusion process. Liquid crystalline nematic domains, for example, form at concentrations as low as 0.5 wt % if the aspect ratio of the anisotropic particles is higher than 100. For CNCs with an aspect ratio of 20, this critical concentration increases to 3 wt %.[52−61] In the absence of flow, particles are locally aligned within the liquid crystal domains, but the different orientation of individual domains leads to a global random distribution of particle orientations. Understanding how these domains reorganize under flow and determine the microstructure during extrusion is crucial for the design of inks and for establishing manufacturing conditions suitable for the 3D printing of composites loaded with anisotropic particles.

DOI: 10.1021/acsnano.8b02366
ACS Nano 2018, 12, 6926−6937

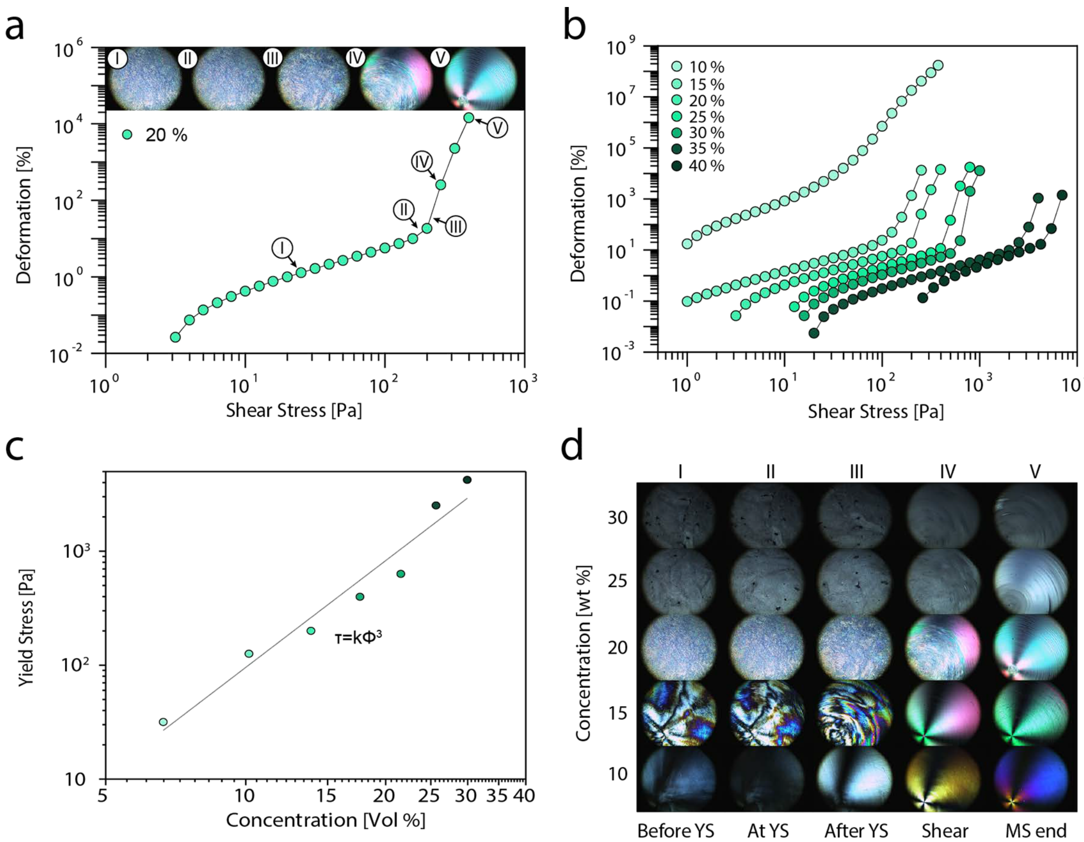

Figure 1. Flow and alignment of CNCs as a function of applied shear stress and cellulose concentration. (a) Yield stress (YS) measurement for a 20 wt % CNC ink and the corresponding polarized images recorded before the yield stress (I), at the yield stress (II), after the yield stress (III–IV), and at the end of the measurement (V). (b) Yield stress measurements of CNC suspensions at 10, 15, 20, 25, 30, 35, and 40 wt %. (c) Yield stress values extracted from (b) for inks with different concentrations of CNCs. The yield stress dependence on the CNC volume fraction is shown to be well described by an experimentally fitted power law. (d) *In situ* rheology imaging as a function of CNC concentration at varying applied shear stresses (I–V).

Here, we use shear-induced polarized light imaging to study the alignment dynamics of cellulose nanocrystals under shear flow in suspensions with high volume fractions of particles. Because of the high volume fractions in the range from 10 to 40 wt %, the investigated CNC inks show a well-defined yield stress and a strong shear thinning behavior. First, we evaluate the effect of the yield stress on the alignment of CNCs under increasing shear deformation. This is followed by steady-state rheological experiments, in which we quantify the degree of alignment over time for suspensions of different CNC volume fractions subjected to varying shear rates. This dependence on shear rates is then utilized to estimate the level of alignment during extrusion if only shear forces are considered. Comparison of these estimates with experiments in model capillaries allows us to propose guidelines for the design of inks and extrusion geometries according to the level of alignment targeted in the final 3D-printed composites. This fundamental understanding sheds light into the possible range of microstructures achievable by direct ink writing of inks containing high concentrations of anisotropic CNC particles, which we introduced in a previous publication.[11]

RESULTS AND DISCUSSION

The dynamics of the orientation of anisotropic particles under shear flow depends on the shear rate imposed on the suspending fluid. In 3D printing by direct ink writing (DIW), the fluid is deposited on a substrate in a spatially controlled manner through the application of an external pressure along the nozzle. Because of wall friction, the shear stresses [τ] arising from the applied pressure are maximal at the nozzle wall and decrease linearly toward the center of the nozzle (Scheme 1). The ink rheological properties determine the characteristic velocity and shear rate profiles that will result from these imposed stresses. Therefore, understanding particle alignment dynamics during the 3D printing process requires a quantitative analysis of the rheological behavior of the ink and of the response of the anisotropic particles to the applied shear rate. For stress-sensitive anisotropic inks, such as cellulose nanocrystal gels, the alignment of particles itself changes the rheological properties of the fluid. This leads to a complex interplay between the ink rheological behavior, the orientation dynamics of particles, and the local shear rates applied through the nozzle. To understand this interdependency, we simplify the problem by studying first the effect of a fixed shear rate profile on the alignment dynamics of cellulose nanocrystals.

Particle alignment dynamics at controlled shear rates is investigated using *in situ* polarization rheology. In this technique, the time-dependent alignment of cellulose nanocrystals can be quantified by optical imaging of the suspension while it is subjected to a well-controlled shear rate in a rheometer (Scheme 1). Because cellulose nanocrystals are optically anisotropic, they display different colors depending on their orientation, when observed between two cross-polarized filters. The observed color depends on the

DOI: 10.1021/acsnano.8b02366
ACS Nano 2018, 12, 6926–6937

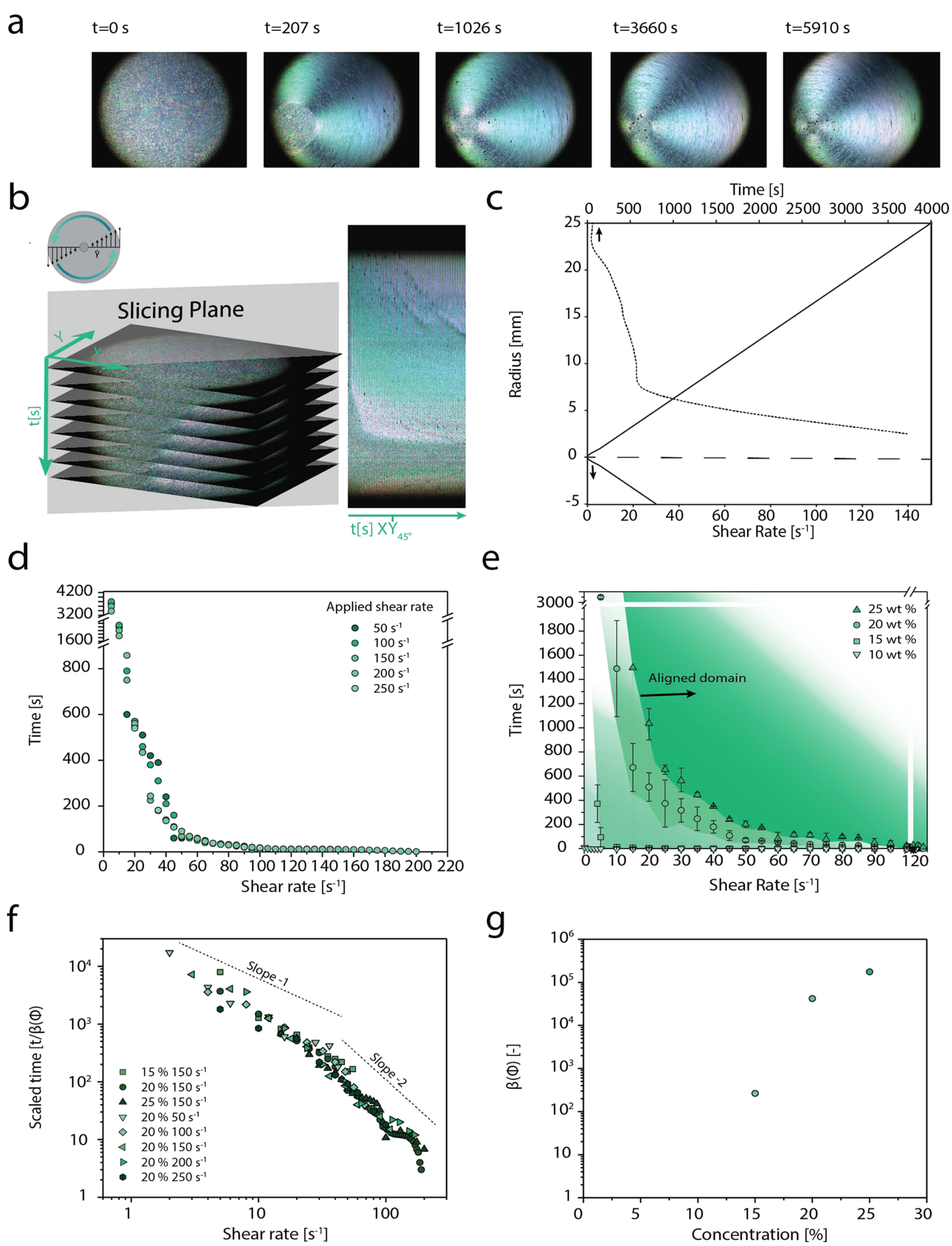

Figure 2. Alignment of CNCs as a function of time for fixed applied shear rates and CNC concentrations. (a) Snapshots taken at different time intervals highlighting the dynamic alignment of a 20 wt % ink at a constant shear rate of 150 s^{-1}. (b) Stack of polarized light images obtained for an ink containing 20 wt % CNC subjected to a constant shear rate of 50 s^{-1}. Vertical slicing of the image stack at an arbitrary angle of $\pm 45°$ enables direct visualization of the alignment process as a function of time. (c) Shear rate distribution in a parallel plate system and the evolution of the alignment time as a function of the plate radius extracted from the sliced stack of pictures. (d) Dependence of the alignment time on the local shear rate for a 20 wt % CNC ink subjected to different maximal applied shear rates (shear rate at the rim). (e) Alignment dynamics diagram displaying the average alignment times as functions of shear rates for different CNC concentrations of 10, 15, 20, and 25 wt %. (f) Log−log master plot of the alignment time as a function of shear rate with corresponding slopes of −1 and −2. (g) Variation of the scaling factor, $\beta(\Phi)$, with the CNC concentration.

orientation and spacing between the individual crystals. As an example, particles exhibiting circumferential orientation around a central axis lead to a characteristic Maltese cross under cross-polarizers (Scheme 1, c_2). The dark and colored areas in this characteristic image emerge from either complete or partial light extinction as it passes through the two polarizers, respectively (see Supporting Information section S4).[41,62]

The alignment of the nanosized cellulose crystals under pure shear flow was measured *in situ* using suspensions with varying

DOI: 10.1021/acsnano.8b02366
ACS Nano 2018, 12, 6926−6937

particle concentrations in a parallel plate geometry. As opposed to the linear increase in shear stress along the radius of the printer's nozzle, rotation of the upper plate leads to a linear increase in shear rate from the center to the rim of the discs. Our experiments show that the lyotropic, needle-shaped cellulose crystals transiently orient from the rim toward the center of the disc in response to the linear gradient in shear rate. This is reflected by the gradual transition in colors (Scheme 1, a_2 to c_2) between the center and the rim of the disc as well as the broadening of the extinction or transmission areas. Note that the camera used to record this transient alignment was placed slightly off-centered to obtain a full view of the side and the middle of the shearing plane. Using this technique, it is possible to track the evolution of alignment quality in CNC suspensions as a function of time for well-defined shear deformations or shear rates.

Our analysis of the alignment of CNC particles using *in situ* polarization rheology was first carried out by applying a constantly increasing shear deformation or shear stress to suspensions containing volume fractions between 10 and 40 wt % of particles. These concentrations lie above the threshold volume fraction beyond which the particles form a space-filling percolating network (see Supporting Information S5). As a result, all the suspensions investigated in this study form a gel with a well-defined yield stress.[63] Because of the high volume fraction used, the CNC particles are also expected to self-assemble into chiral nematic domains throughout the suspension.[37,61,64−66] The formation of nematic domains was experimentally confirmed for suspensions containing more than 10 wt % CNCs (Figures S.2 and S.6).

Flow-induced alignment of the particles is therefore only possible if the applied stress surpasses the yield stress of the suspension. Indeed, our measurements show that the shear stresses at which the initial color pattern starts to change in the cross-polarized images are in good agreement with the yield stress of the gel detected through the inflection point in the rheological flow curve. Because the shear stress scales with the shear deformation at low rotational displacements, the shear stress applied in these measurements increases linearly from the center to the rim of the disc. The nominal shear stresses reported here correspond to the stress applied at the plate's rim. Taking a suspension with 20 wt % CNC as an example, no preferential orientation of particles is observed under cross-polarized light when the shear stress applied at the rim is lower than the yield stress of the gel (Figure 1a, I). But if the nominal yield stress value of 200 Pa is reached at the rim, the gel starts to flow and CNC orientation is observed at this outer region of the plate (II). The fraction of aligned CNCs increases as the local shear stress progressively increases (III−IV). Eventually, higher stress levels result in CNC alignment along the rotation direction throughout the whole probed volume (V).

The yield stress of the CNC suspensions was found to increase significantly from 30 to 4220 Pa as the concentration of particles increased from 10 to 40 wt % (Figure 1b). This dependence can be described by the simple power law $\tau_y = k\phi^p$, where τ_y is the yield stress of the gel, ϕ is the volume fraction of particles, k is a constant that depends on the interparticle interactions and particle size, and p is an exponent that depends on the microstructure of the particle network. The exponent $p = 3$ obtained by fitting the measured data with the power law function lies within the range 1.4−5.0 typically found in the literature (Figure 1c; see also Supporting Information S5).[67,68]

The observed power law dependence of the yield stress on the volume fraction of particles is often interpreted in terms of the underlying microstructure of the load-bearing particle network.[69] In the case of spherical particles, the network is usually formed by fractal-like agglomerates that connect to each other to fill up the entire volume of the suspension. Such agglomerates are larger and less dense if the volume fraction of particles is lower. By contrast, higher particle volume fractions lead to smaller and denser agglomerates. In analogy to fractal-like agglomerates, our yield stress data suggest that the formation of load-bearing structural units of different sizes and densities depend on the CNC concentration. Indeed, the size of nematic domains was observed to decrease with increasing concentrations of CNCs in the suspension (Figure 1d). At the lowest concentration of 10 wt %, large domains are clearly visible. Increasing the CNC weight fraction to 15 and 20 wt % leads to smaller domains with distinct alignment directions. Above 20 wt %, these domains become even smaller and are no longer easily visible by optical microscopy (Figure 1d). This interpretation is supported by earlier studies that showed a decrease of the interparticle spacing within liquid crystalline phases with increasing particle volume fraction.[24,70,71]

Once the yield stress of the CNC suspension is reached, particles are expected to align parallel to the imposed shear forces. Since the alignment process of particles in highly concentrated suspensions is poorly understood, we investigate the effect of the imposed shear rates on the alignment dynamics of particles in suspensions with varying CNC concentrations. This was experimentally accomplished by exploiting the linear radial distribution of the shear rate applied in the parallel plate geometry used for the rheological measurements. Because of this linear distribution, the alignment time at different shear rates can be directly assessed in one single measurement at a constant global rotational speed of the plate.

The time-dependent alignment process for a 20 wt % CNC suspension at a fixed global rotational speed of the plate is shown in Figure 2a. The global rotation speed is indicated in terms of the maximum shear rate at the rim of the plate, which in this example was kept constant at 150 s^{-1}. The cross-polarized snapshots reveal that alignment starts at the rim of the plate and progresses toward the center of the plate, in response to the imposed linear gradient in shear rate. The alignment time at one given shear rate can thus be directly assessed from the optical images. To demonstrate the alignment dynamics visually, polarizing light images were taken at precise time intervals and stacked into a 3D image (Figure 2b and Supporting Information S6). Extracting a vertical slice of such 3D image allows us to directly determine the alignment time as a function of local shear rate (Figure 2c). By repeating this procedure for different suspensions and distinct maximal applied shear rates, it was possible to determine the alignment time for a wide range of shear rates and CNC concentrations (Figure 2d,e). Because of the linear shear rate distribution, the alignment time data overlap into a single curve regardless of the maximal shear rate applied. This confirms that the alignment time is solely governed by the local shear rate rather than the maximum applied shear rate (Figure 2d). Plotting the alignment time data obtained at different particle concentrations, we obtain a design diagram that indicates the minimum time and shear rate necessary to induce alignment of the CNCs under shear flow (Figure 2e).

DOI: 10.1021/acsnano.8b02366
ACS Nano 2018, 12, 6926−6937

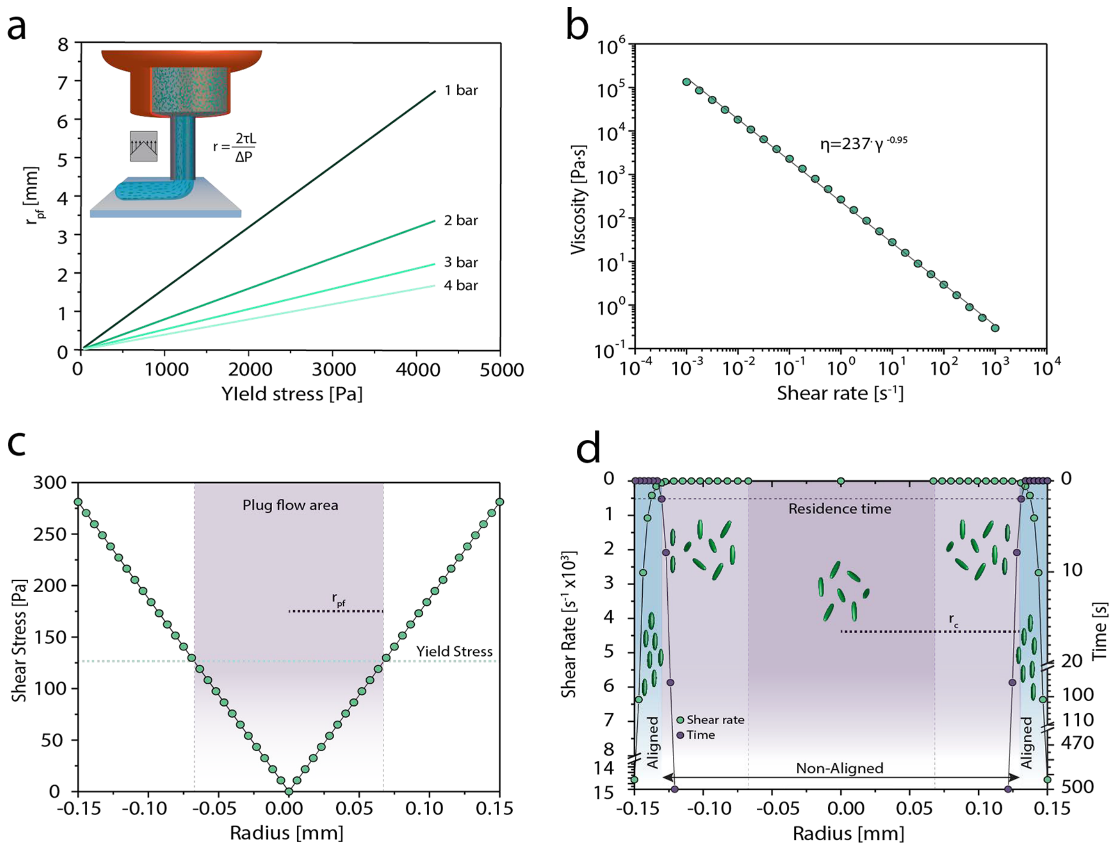

Figure 3. Estimation of shear-induced particle alignment expected during 3D printing of an exemplary ink containing 15 wt % CNC. (a) General dependence of the plug-flow radius (r_{pf}) on the yield stress of the ink for different applied pressures, assuming a printing needle with a diameter of 0.3 mm and length of 80 mm. (b) Flow curve for the 15 wt % ink and its description using a power law fit. (c) Shear stress distribution across the radius of a nozzle with 80 mm length and 0.3 mm diameter. The yield stress of the 15 wt % CNC ink is also indicated to show the plug-flow area of the nozzle. (d) Shear rate profile and corresponding alignment times along the nozzle radius. The residence time of the 15 wt % CNC ink is also shown to establish the differential flow domain and the region of the nozzle where shear-induced alignment of the particles is expected.

Our experimental results reveal that the alignment time at a given shear rate is strongly influenced by the concentration of CNC particles. For example, the alignment time at 20 s^{-1} increases approximately 2-fold if the CNC concentration increases from 20 to 25 wt %. The alignment of CNCs under shear flow is accompanied by significant changes in the microstructure and rheological properties of the suspension (Supporting Information S6 and S7). The longer alignment times measured for concentrated suspensions is probably related to the stronger steric and hydrodynamic interactions between particles at high CNC volume fractions (Figure 2e and Supporting Information S6 and S7). Following the interpretation provided to explain the yield stress data, the alignment dynamics should be affected by the size and density of the nematic domains formed within the suspension. At the low concentrations ranging from 10 to 15 wt %, the larger nematic domains formed by the CNC crystals are less dense and easier to break and align under external shear. This phenomenon is also typically observed in liquid crystals.[50,72] The much smaller and denser domains formed at concentrations above 20 wt % are more difficult to rupture and thus require shearing for longer times to achieve particle alignment (Figures S.5−7).

Besides the effect of CNC concentration on alignment times, our experimental results also provide insights into the dependence of the alignment dynamics on the applied shear rate. According to predictions for an isolated anisotropic particle suspended in a Newtonian fluid, the time it takes for the particles to align (t) is inversely proportional to the applied shear rate ($\dot{\gamma}$).[32] However, it is questionable whether this simple scaling relation also holds true for a particle assembled within a nematic domain of the complex multidomain microstructure obtained at high CNC volume fractions. To address this question, we combined all the experimental data obtained from our transient shearing tests in a single log−log plot displaying the alignment time as a function of the applied shear rate (Figure 2f). To account for the slower alignment process in suspensions with higher CNC volume fractions, the alignment time was scaled with a constant term β that should capture the effect of steric and hydrodynamic interactions on particle reorientation under shear. In this analysis, β depends only on the volume fraction of particles (Figure 2g), leading to the following relation:

$$t = \frac{\beta(\phi)}{\dot{\gamma}} \qquad (1)$$

This simple scaling describes quite well the dynamics of the alignment process, since all the experimental data were found to fall in a single master curve in the log−log plot (Figure 2f). Analysis of the slope of the resulting master curve allows us to compare the effect of shear rate on alignment dynamics in concentrated suspensions with the dependence expected for a

DOI: 10.1021/acsnano.8b02366
ACS Nano 2018, 12, 6926−6937

model single particle. Surprisingly, we observe that the slope of −1 expected for a single particle provides a good approximation of the shear rate dependence of the alignment times at low shear rates. This suggests that, if the applied shear rates are low, the simple relation $t \sim 1/\dot{\gamma}$ is still a reasonable approximation even if particles are part of crystalline domains at high volume fractions. By contrast, the alignment time shows a stronger shear rate dependence when higher shear rates are applied. In this case, we find that the alignment time scales with $1/\dot{\gamma}^2$. This indicates that in concentrated inks subjected to high shear rates particles align faster than expected for a diluted suspension. Although further work is needed to explain the underlying physics giving rise to this unusual scaling relation, such a stronger effect of the shear rate suggests that hydrodynamic and steric interactions between the particles at high volume fractions and high shear rates might facilitate their alignment by shear. Such interparticle interactions increase significantly with the CNC volume fractions, which is reflected in higher values for the scaling factor beta $\beta(\Phi)$ (Figure 2g). It is important to note that the above physical description of the alignment dynamics should be universal and applicable to other concentrated colloidal systems, as long as the anisotropic particles interact repulsively like the model CNC particles used in our experiments. Our analysis might also be applicable to more complex fluids containing distinct types of particles, if such particles are sufficiently different in size to enable a coarse-grained description in which the larger particles are assumed to be suspended in a homogeneous fluid containing the smaller particles. Beyond these simplifying assumptions, this study provides a basis for future investigations of the alignment dynamics in more complex colloidal suspensions containing for example several types of particles that interact through attractive and repulsive forces.

Our understanding of the effect of particle concentration on the yield stress and alignment dynamics allows us to estimate the contribution of shear flow alone on the alignment of anisotropic particles during 3D printing. Using a glass capillary as model nozzle and pressures within the range applied for direct ink writing, we evaluate the level of particle alignment expected throughout the nozzle radius (Supporting Information S8). The quartz capillaries used have a diameter ($2R$) and length (L) of 0.3 mm and 80 mm, respectively. Since the CNC inks exhibit a finite yield stress (Figure 1a−c), a fraction of the material will not experience any shear flow during extrusion. This fraction is located in the inner core of the extrudate, where the shear stress applied is lower than the yield stress of the ink. By comparing the yield stress of the ink with the linear change in shear stress along the nozzle radius, one can obtain the critical radius below which the material will not experience shear flow. We call this critical radius the plug-flow radius (r_{pf}). The plug-flow radius depends on the yield stress of the ink, on the geometry of the nozzle, and the pressure applied during printing. For a given nozzle length and applied pressure, r_{pf} increases linearly with the yield stress of the ink (Figure 3a).

Between the plug-flow radius (r_{pf}) and the nozzle radius (R), the ink experiences shear flow. This leads to the so-called differential flow region, where shear-induced alignment of the anisotropic particles may occur. The level of particle alignment within the differential flow region of the nozzle can be estimated from the alignment time data obtained from the opto-rheological measurements. To this end, we must first determine the local shear rate imposed on the ink as a function of the nozzle radius. This is possible by translating the linear shear stress profile across the nozzle radius into a shear rate profile using the rheological behavior of the ink. As an illustrative example, we estimate the shear rate profile for an exemplary ink containing 15 wt % of CNC particles (Figure 3c) and subjected to a pressure of 3 bar through a model nozzle. The shear rate is given by the derivative of the velocity profile, which is strongly influenced by the rheological properties of the ink. We find that the following simple power law describes well the shear-thinning behavior of the ink (Figure 3b): $\eta = k\,\dot{\gamma}^{n-1}$, where η is the viscosity, k is the flow consistency index, and n is the flow behavior index. The obtained flow index n of this 15 wt % ink is on the same order of magnitude as the values observed for CNFs and diluted CNC suspensions.[64,73] Such a low n value reflects the strong shear thinning nature of the ink. Using such a rheological description, the geometry of the nozzle, and the pressure applied, we calculated the shear profile expected during extrusion of the ink with 15 wt % CNC (Figure 3d and Supporting Information S8 and S9).

Once the shear rate profile is known, one can use eq 1 to estimate the alignment time expected for different radii across the nozzle. Comparison of this alignment time with the residence time in the nozzle finally leads to the critical radius, r_c, above which particle alignment is expected within the differential flow region (Figure 3d). By combining eq 1 with the estimated residence time and shear rate profile we find the following prediction for the critical radius (Supporting Information S9):

$$\frac{r_c}{R} = \left[\frac{R\beta(\Phi)n}{L(3n+1)}\right]^n \tag{2}$$

Such a relation neglects any time dependence of the rheological properties of the ink. This is a reasonable assumption for the inks investigated in this work, in view of the relatively weak change of their viscosity as a function of time (Supporting Information Figure S.4).

The identified plug-flow (r_{pf}) and critical (r_c) radii eventually define three distinct flow regions within the nozzle. This is illustrated in Figure 3d for the exemplary ink with 15 wt % CNCs. The dark purple area displays the plug flow region where no shear occurs (r_{pf} = 0.0672 mm). The light purple and blue areas highlight the differential flow region. Alignment due to shear forces alone is expected within the blue area. Because of the relatively short residence time (2 s for this capillary) and strong non-Newtonian nature of the ink, high shear rates are only exerted very close to the nozzle's wall. For this 15 wt % ink, we estimate the relative critical radius (r_c/R) to be around 0.83. This means that shear-induced alignment of the CNC particles of this ink is expected to occur within a distance of 25 μm from the nozzle wall. Such an aligned region corresponds to 27% of the total volume of the filament. Following this rationale, eq 2 can be used to estimate the region of shear-induced alignment for other nozzle geometries, ink compositions, and printing conditions. The same reasoning can be repeated with 3D printing needles of different geometries (Supporting Information S9).

To qualitatively validate the above prediction, we performed additional experiments in which a 15 wt % CNC suspension is forced through a long glass needle at a fixed pressure, thus simulating the extrusion process. The experimental setup was designed to ensure that only shear deformation is imposed on

DOI: 10.1021/acsnano.8b02366
ACS Nano 2018, 12, 6926−6937

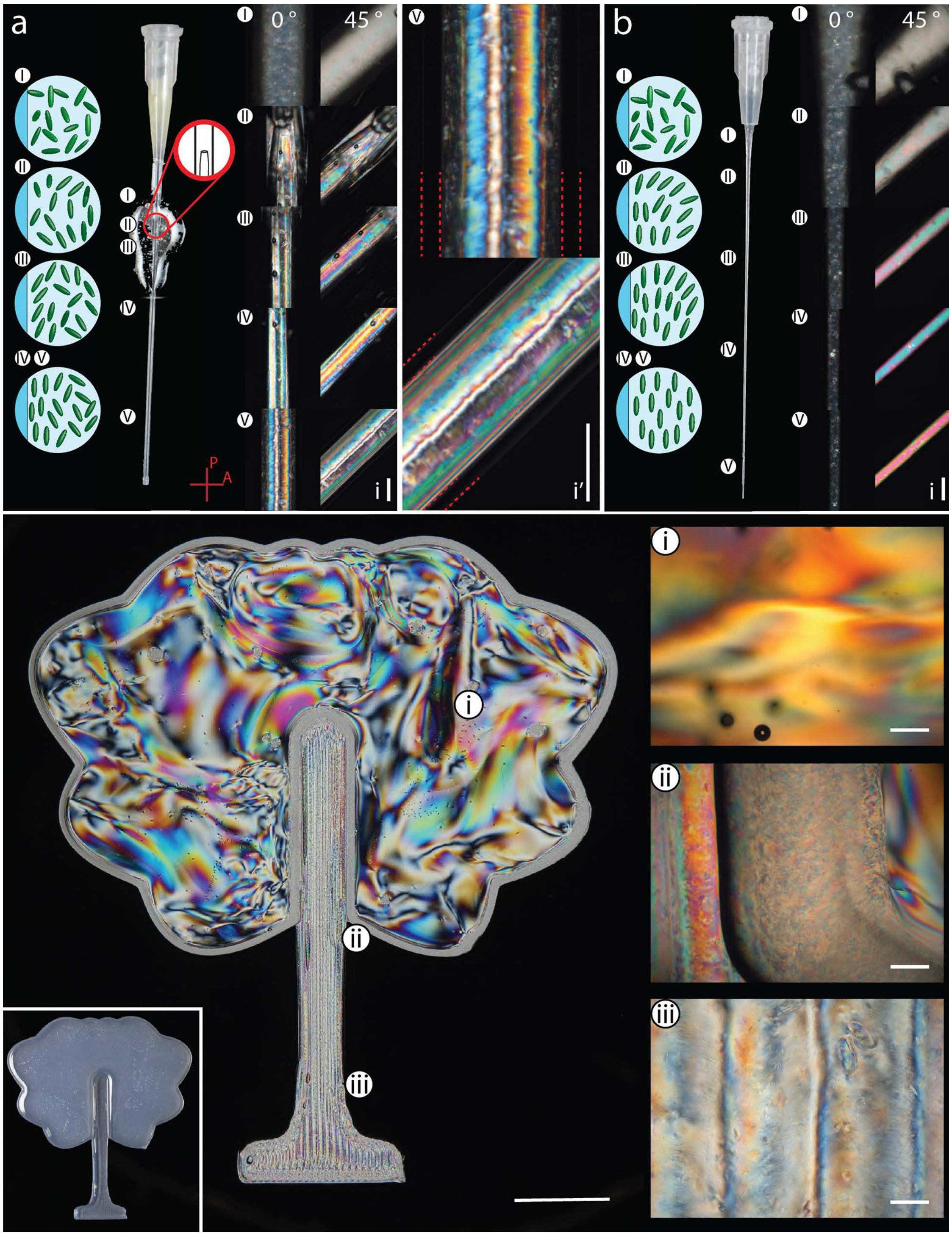

Figure 4. Visual assessment of CNC alignment during extrusion of a 15 wt % ink through model capillaries and an artistic illustration of our ability to locally control the orientation of printed CNC particles. (a) Polarized light imaging along a quartz capillary designed to ensure pure shear flow during extrusion. The diverging tapered geometry of the inner capillary erases possible previous alignment of particles caused by extensional flow. Extrusion was carried out at 3 bar. Polarized images captured at 0° and 45° orientation with respect to analyzer filter indicate the level of alignment of the CNC particles along the capillary length. Scale bar i: 500 μm. The zoom-in of section V highlights the alignment of CNC particles close to the capillary wall. Scale bar i′: 500 μm. The walls of the capillary are indicated by dashed red lines. (b) Polarized light imaging at angles 0° and 45° along a quartz capillary with a converging tapered section (extrusion at 3 bar). Scale bar i: 500 μm. (c) Printed tree created using different inks and imaged by cross-polarized light. Scale bar: 1 cm. The inset on the left shows the tree pattern under normal illumination. OM images of selected areas containing inks with different compositions deposited with distinct approaches: (i) 10 wt % casted, (ii) interfaces between 15 and 20 wt % printed inks (left), and 20 wt % printed and 10 wt % casted (right), and (iii) 15 wt % printed. Scale bar of zoomed-in sections: 200 μm.

DOI: 10.1021/acsnano.8b02366
ACS Nano 2018, 12, 6926−6937

the suspension during extrusion. This was achieved by constructing a capillary device that features a widening diameter at the entrance (Figure 4a). Such widening leads to an abrupt decrease in flow velocity, thus generating extensional forces that erase any alignment previously imposed to the particles.[74,75] Using such a device, we assessed the level of alignment of the CNC particles by taking cross-polarized optical images at different positions along the length of the glass capillary. The experiment confirms that the CNC particles are aligned only within an outer skin of the ink close to the wall of the capillary. This is clearly indicated by the darker region next to the glass wall when the capillary is observed under cross polarizers (Figure 4a, V).

The observation that shear-induced alignment is restricted to the skin of the printed filament contrasts with previous studies in which stronger particle alignment has been achieved by direct ink writing.[9,11,13] To reconcile these observations, we conducted additional alignment experiments in capillaries with a tapered geometry. Such geometry imposes extensional flow along the entire capillary length and is representative of the shape of some of the nozzles used for direct ink writing. Extensional flow is known to be an effective means to impose orientation in anisotropic fluids.[25,29,76] Indeed, our results reveal that strong alignment is achieved along the entire cross-section of the capillary if extensional flow is imposed on the CNC suspension (Figure 4b).

The ability to spatially tune the level of alignment of anisotropic particles through changes in the nozzle geometry, the rheological properties of the ink, and the printing operating conditions provides a wide design space for the fabrication of printed objects with controlled site-specific particle orientation. This increases the pallet of possible microstructural libraries that are accessible *via* 3D printing of anisotropic particles. Different types of microstructures are needed depending on the properties required in the end function or application. Exploiting a broad range of microstructural designs to manipulate local properties is the strategy used by many living organisms to cope with the functional demands of their living environment using a limiting number of building blocks.[77,78] Following this rationale, one would expect that filaments with alignment restricted to the skin might combine interesting antagonistic properties, such as high wear resistance and high stretchability. Like the Byssus threads produced by mussels, these properties would arise from the combination of a softer inner core and a stiffer outer layer. By contrast, filaments containing anisotropic particles fully aligned within the entire cross-section would enable maximum reinforcement in specific directions subjected to the highest mechanical loads. This is a common design strategy in Nature to create strong and stiff materials, such as those in the nacreous layer of mollusk shells.

We visually demonstrate this concept of tunable local structuring by 3D printing and casting a colorful tree pattern consisting only of CNC particles as building blocks (Figure 4c). In this artistic representation, the center of the tree consists of a 10 wt % ink with large and colorful nematic domains, whereas the trunk consists of a 15 wt % CNC ink extruded along a specific direction to locally align the CNC particles. Besides these two local microstructures, the outline of the tree crown consists of a 20 wt % ink where the CNC particles are expected to align only very close to the filament surface.

CONCLUSIONS

The level of particle alignment achieved through extrusion-based 3D printing of cellulose-containing inks can be varied widely depending on the rheological properties of the ink and the type of flow imposed during the printing process. Filament architectures comprising an aligned shell around a randomly oriented core are typically produced under pure shear conditions, whereas stronger alignment is observed if the printing nozzle geometry is designed to also induce extensional flow. The first condition required for particle alignment under pure shear flow is that the applied shear stresses overcome the yield stress of the ink. Once this condition is satisfied, the time required for the alignment of anisotropic particles under shear can be quantified using a simple scaling relation that takes into account the shear rate applied and interactions between the particles at different volume fractions. At low applied shear rates, a linear dependence between the alignment time and the inverse of the shear rate was found to be a good approximation for the alignment dynamics. Deviation from this linear dependence is found at higher shear rates, where steric and hydrodynamic interactions between particles are expected to play a stronger role. Although further work is required to fully elucidate the effect of particle concentration on the alignment dynamics, our study offers quantitative parameters for the design of nozzle dimensions, printing conditions, and rheological properties required to tune the shear-induced orientation of anisotropic particles during 3D printing of composite inks.

EXPERIMENTAL METHODS

Sample Preparation. Cellulose nanocrystals were prepared *via* sulfuric acid hydrolysis of eucalyptus pulp at the USDA Forest Service, Forest Products Laboratory (Madison, WI, USA), according to a published procedure.[56] Freeze-dried CNCs (0.98 wt % sulfur content) with a measured length of 100 ± 40 nm and a diameter of 6.5 ± 2 nm (TEM image in Supporting Information Figure S.1) were dispersed in water at different concentrations, ranging from 10 wt % up to 40 wt % and mixed for 5 min at 2500 and 3500 rpm, respectively, with a speed mixer (model DAC 150.1 FVZ). Previous work on these CNC particles has shown that they exhibit zeta potentials in the range of −40 to −45 mV when suspended in water containing 10 mM NaCl.[79] This high electrical potential results in repulsive forces between the particles in the aqueous medium. The resulting CNC gel was left overnight for swelling, mixed at 3500 rpm for 5 min, and stored in a refrigerator prior to testing. Before the measurements the samples were premixed at 3500 rpm for 5 min.

Transmission Electron Microscopy. Cellulose nanocrystals were characterized by transmission electron microscopy (TEM, Jeol JEM-2200FS, USA Inc.) using an acceleration voltage of 200 kV. Plasma-activated carbon-coated grids were used as support onto which a 0.02 wt % diluted suspension of the cellulose nanocrystals was deposited and stained with a 2 wt % solution of uranyl acetate for 30 s. The average lengths and diameters of CNCs were measured with the software ImageJ.

Rheology. The rheometer setup (Anton Paar MCR502) was modified with a reflection polariscope known as shear-induced polarized light imaging to enable *in situ* polarization microscopy. In this setup, the shearing plate acts simultaneously as optical mirror (roughness about 1 μm) and rheological shearing tool. A Peltier temperature control unit with a transparent bottom plate (P-PTD 200/Gl) and a corresponding Peltier-controlled hood (H-PTD 200) provides a uniform temperature distribution and optical access to the sample.

Working with a high-intensity white light source, the LED light is projected onto the beam splitter of the polariscope after passing a first homogenizing filter, a collimating lens, and the first linear polarizer

DOI: 10.1021/acsnano.8b02366
ACS Nano 2018, 12, 6926−6937

(0°), as shown in Scheme 1b. The beam splitter reflects the incident beam of the light source toward the sample and transmits its reflection toward a second series of lenses and an orthogonally oriented linear polarizer (90°) onto the HR camera. A detailed description of this setup and approach was previously reported by Mykhaylyk *et al.* and Völker-Pop.[41,47]

Measurements were carried out using a parallel plate (50 mm diameter) gap of 0.2 mm (unless specified otherwise) and at a constant temperature of 20 °C. The gap was chosen to enable visualization of CNC alignment. Higher gap sizes and acquisition times were shown to give equivalent results in preliminary rheological tests (Supporting Information Figure S.3). Differences between the rheological properties obtained using cone-plate and parallel plate geometries were also found to be minimal in shear sweep measurements (Supporting Information Figure S.4).

Yield stress measurements were performed in rotation under increasing shear stresses from 0.01 to 1000 Pa for concentrations below 30 wt %. Shear stresses up to 2000 Pa were applied for concentrations above 30 wt %. Using time intervals of 25 s for each data point, a total of 34 points were acquired during these stress sweep tests.

Flow curves under shear rates ranging from 10 to 350 s^{-1} were obtained through time-controlled measurements. Time sweeps at constant shear rates were performed using time intervals of 4.5 s per measuring point.

Image Processing. Images were processed using the software FIJI (ImageJ) V.1.51h.

3D Printing. Printing experiments were performed using the Bioplotter Manufacturing series from EnvisionTEC. The material was extruded under controlled pressure ranging from 0.5 to 1.2 bar depending on the needle and material concentration.

Nozzles with different dimensions and geometries were prepared to study particle alignment under an optical microscope by using 80 mm long and 0.3 mm diameter quartz capillaries from Hilgenberg. The capillaries were mounted on the printer by connecting them to standard DIW needles using an adapter obtained from Nordson. The tapered capillary utilized to demonstrate the effect of extensional forces on particle alignment was prepared by connecting two circular glass capillaries with different inner diameters of 2 and 0.5 mm, respectively (World Precision Instruments). The tapered section was produced by hot pulling (Sutter Instrument Co., model p97). The capillaries were held together with double-component epoxy glue.

The tree pattern was printed using inks containing 10, 15, and 20 wt % of CNC particles. Inks loaded with 15 and 20 wt % CNC were used to build the contour and the trunk, whereas the 10 wt % ink was casted within the boundaries of the printed contour.

Optical Microscopy. All optical microscopy analyses were performed on an Axioplan microscope from Zeiss equipped with cross-polarized filters. The capillaries were placed between the polarized filters for imaging.

ASSOCIATED CONTENT

Supporting Information

The Supporting Information is available free of charge on the ACS Publications website at DOI: 10.1021/acsnano.8b02366.

> Electron microscopy images of CNCs, polarized light images of suspensions, additional yield stress measurements, additional flow curves, percolation analysis of concentrated suspensions, additional alignment dynamic images, progression of aligned area with time, effect of shear rates on viscosity, time, and concentration; additional information on plug-flow and analysis of flow behavior of fluids (PDF)

AUTHOR INFORMATION

Corresponding Authors

*E-mail: patrick.ruehs@mat.ethz.ch.
*E-mail: gilberto.siqueira@empa.ch.
*E-mail: andre.studart@mat.ethz.ch.

ORCID

Michael K. Hausmann: 0000-0001-8187-425X
Patrick A. Rühs: 0000-0003-1918-8253
André R. Studart: 0000-0003-4205-8545

Notes

The authors declare no competing financial interest.

ACKNOWLEDGMENTS

We thank P. Fischer for the scientific contribution and advice, J. Kohlbrecher for providing the additional rheometer, L. Völker-pop for the logistics between Anton Paar and ETH, E. Jeoffroy and A. Demirörs for the scientific discussions, and A. Huch for the TEM imaging. P.A.R. and A.R.S. greatly acknowledge the financial support from the Swiss National Science Foundation (consolidator grant number BSCGI0_157696). R.L. is thankful for the financial support from the Swiss Competence Center for Energy Research SCCER Mobility and the Swiss Innovation Agency Innosuisse. M.K.H. and G.D.S. greatly acknowledge the financial support from the Swiss National Science Foundation (200021_159906/1). This work also benefitted from support from the Swiss National Science Foundation through the National Center of Competence in Research Bio-Inspired Materials.

REFERENCES

(1) Compton, B. G.; Lewis, J. A. 3D-Printing of Lightweight Cellular Composites. *Adv. Mater.* **2014**, *26*, 5930−5.
(2) Studart, A. R. Additive Manufacturing of Biologically-Inspired Materials. *Chem. Soc. Rev.* **2016**, *45*, 359−76.
(3) Gross, B. C.; Erkal, J. L.; Lockwood, S. Y.; Chen, C.; Spence, D. M. Evaluation of 3d Printing and Its Potential Impact on Biotechnology and the Chemical Sciences. *Anal. Chem.* **2014**, *86*, 3240−53.
(4) Khoo, Z. X.; Teoh, J. E. M.; Liu, Y.; Chua, C. K.; Yang, S. F.; An, J.; Leong, K. F.; Yeong, W. Y. 3D Printing of Smart Materials: A Review on Recent Progresses in 4d Printing. *Virtual Phys. Prototy* **2015**, *10*, 103−122.
(5) Schaffner, M., Rühs, P. A., Coulter, F.; Kilcher, S.; Studart, A. R. 3D Printing of Bacteria into Functional Complex Materials. *Sci. Adv.*, **2017**, *3*, eaao6804.
(6) Farahani, R. D.; Chizari, K.; Therriault, D. Three-Dimensional Printing of Freeform Helical Microstructures: A Review. *Nanoscale* **2014**, *6*, 10470−10485.
(7) Kokkinis, D.; Schaffner, M.; Studart, A. R. Multimaterial Magnetically Assisted 3D Printing of Composite Materials. *Nat. Commun.* **2015**, *6*, 8643.
(8) Martin, J. J.; Riederer, M. S.; Krebs, M. D.; Erb, R. M. Understanding and Overcoming Shear Alignment of Fibers During Extrusion. *Soft Matter* **2015**, *11*, 400−405.
(9) Feilden, E.; Ferraro, C.; Zhang, Q.; Garcia-Tunon, E.; D'Elia, E.; Giuliani, F.; Vandeperre, L.; Saiz, E. 3D Printing Bioinspired Ceramic Composites. *Sci. Rep.* **2017**, *7*, 13759.
(10) Martin, J. J.; Fiore, B. E.; Erb, R. M. Designing Bioinspired Composite Reinforcement Architectures Via 3D Magnetic Printing. *Nat. Commun.* **2015**, *6*, 8641.
(11) Siqueira, G., Kokkinis, D.; Libanori, R.; Hausmann, M. K.; Gladman, A. S.; Neels, A.; Tingaut, P.; Zimmermann, T.; Lewis, J. A.; Studart, A. R. Cellulose Nanocrystal Inks for 3D Printing of Textured Cellular Architectures. *Adv. Funct. Mater.*, **2017**, *27*, 1604619.
(12) Lewis, J. A. Direct Ink Writing of 3d Functional Materials. *Adv. Funct. Mater.* **2006**, *16*, 2193−2204.

DOI: 10.1021/acsnano.8b02366
ACS Nano 2018, 12, 6926−6937

(13) Sydney Gladman, A., Matsumoto, E. A.; Nuzzo, R. G.; Mahadevan, L.; Lewis, J. A. Biomimetic 4D Printing. *Nat. Mater.*, **2016**, *15*, 413.
(14) Collino, R. R.; Ray, T. R.; Friedrich, L. M.; Cornell, J. D.; Meinhart, C. D.; Begley, M. R. Scaling Relationships for Acoustic Control of Two-Phase Microstructures During Direct-Write Printing. *Mater. Res. Lett.* **2018**, *6*, 191−198.
(15) Siqueira, G.; Bras, J.; Dufresne, A. Cellulosic Bionanocomposites: A Review of Preparation, Properties and Applications. *Polymers* **2010**, *2*, 728−765.
(16) Ansari, F.; Sjöstedt, A.; Larsson, P. T.; Berglund, L. A.; Wågberg, L. Hierarchical Wood Cellulose Fiber/Epoxy Biocomposites − Materials Design of Fiber Porosity and Nanostructure. *Composites, Part A* **2015**, *74*, 60−68.
(17) Favier, V.; Chanzy, H.; Cavaille, J. Y. Polymer Nanocomposites Reinforced by Cellulose Whiskers. *Macromolecules* **1995**, *28*, 6365−6367.
(18) Siro, I.; Plackett, D. Microfibrillated Cellulose and New Nanocomposite Materials: A Review. *Cellulose* **2010**, *17*, 459−494.
(19) Habibi, Y. Key Advances in the Chemical Modification of Nanocelluloses. *Chem. Soc. Rev.* **2014**, *43*, 1519−42.
(20) Habibi, Y.; Lucia, L. A.; Rojas, O. J. Cellulose Nanocrystals: Chemistry, Self-Assembly, and Applications. *Chem. Rev.* **2010**, *110*, 3479−3500.
(21) Moon, R. J.; Martini, A.; Nairn, J.; Simonsen, J.; Youngblood, J. Cellulose Nanomaterials Review: Structure, Properties and Nanocomposites. *Chem. Soc. Rev.* **2011**, *40*, 3941−3994.
(22) Zimmermann, T.; Pöhler, E.; Geiger, T. Cellulose Fibrils for Polymer Reinforcement. *Adv. Eng. Mater.* **2004**, *6*, 754−761.
(23) Endes, C.; Camarero-Espinosa, S.; Mueller, S.; Foster, E. J.; Petri-Fink, A.; Rothen-Rutishauser, B.; Weder, C.; Clift, M. J. D. A Critical Review of the Current Knowledge Regarding the Biological Impact of Nanocellulose. *J. Nanobiotechnol.* **2016**, *14*, 78.
(24) Schütz, C.; Agthe, M.; Fall, A. B.; Gordeyeva, K.; Guccini, V.; Salajková, M.; Plivelic, T. S.; Lagerwall, J. P. F.; Salazar-Alvarez, G.; Bergström, L. Rod Packing in Chiral Nematic Cellulose Nanocrystal Dispersions Studied by Small-Angle X-Ray Scattering and Laser Diffraction. *Langmuir* **2015**, *31*, 6507−6513.
(25) Håkansson, K. M. O.; Fall, A.B.; Lundell, F.; Yu, S.; Krywka, C.; Roth, S. V.; Santoro, G.; Kvick, M.; Prahl Wittberg, L.; Wågberg, L.; Söderberg, L. D. Hydrodynamic Alignment and Assembly of Nanofibrils Resulting in Strong Cellulose Filaments. *Nat. Commun.* **2014**. *5*, DOI: 10.1038/ncomms5018.
(26) Scales, P. J.; Johnson, S. B.; Healy, T. W.; Kapur, P. C. Shear Yield Stress of Partially Flocculated Colloidal Suspensions. *AIChE J.* **1998**, *44*, 538−544.
(27) Yanez, J. A.; Shikata, T.; Lange, F. E.; Pearson, D. S. Shear Modulus and Yield Stress Measurements of Attractive Alumina Particle Networks in Aqueous Slurries. *J. Am. Ceram. Soc.* **1996**, *79*, 2917−2924.
(28) Santos de Oliveira, I. S.; van den Noort, A.; Padding, J. T.; den Otter, W. K.; Briels, W. J. Alignment of Particles in Sheared Viscoelastic Fluids. *J. Chem. Phys.* **2011**, *135*, 104902.
(29) Håkansson, K. Orientation of Elongated Particles in Shear and Extensional Flow. In *Trita-MEK*, KTH Royal Institute of Technology; Stockholm, 2012.
(30) Jeffrey, D. J.; Acrivos, A. The Rheological Properties of Suspensions of Rigid Particles. *AIChE J.* **1976**, *22*, 417−432.
(31) Jeffery, G. B. The Motion of Ellipsoidal Particles Immersed in a Viscous Fluid. *Proc. R. Soc. London, Ser. A* **1922**, *102*, 161−179.
(32) Mewis, J.; Wagner, N. J. *Colloidal Suspension Rheology*; Cambridge Series in Chemical Engineering; Cambridge University Press: Cambridge, 2011.
(33) Marrucci, G.; Greco, F. Flow Behavior of Liquid Crystalline Polymers. In *Advances in Chemical Physics*; John Wiley & Sons, Inc., 2007; pp 331−404.
(34) Mueller, S.; Llewellin, E. W.; Mader, H. M. The Rheology of Suspensions of Solid Particles. *Proc. R. Soc. London, Ser. A* **2010**, *466*, 1201−1228.
(35) Orgéas, L.; Dumont, P.; Corre, S. L. 5 - Rheology of Highly Concentrated Fiber Suspensions A2 - Chinesta, Francisco. In *Rheology of Non-Spherical Particle Suspensions*; Ausias, G., Ed.; Elsevier, 2015; pp 119−166.
(36) Correa-Duarte, M. A.; Grzelczak, M.; Salgueirino-Maceira, V.; Giersig, M.; Liz-Marzan, L. M.; Farle, M.; Sierazdki, K.; Diaz, R. Alignment of Carbon Nanotubes under Low Magnetic Fields through Attachment of Magnetic Nanoparticles. *J. Phys. Chem. B* **2005**, *109*, 19060−19063.
(37) Orts, W. J.; Godbout, L.; Marchessault, R. H.; Revol, J. F. Enhanced Ordering of Liquid Crystalline Suspensions of Cellulose Microfibrils: A Small Angle Neutron Scattering Study. *Macromolecules* **1998**, *31*, 5717−5725.
(38) Gorsche, C.; Koch, T.; Moszner, N.; Liska, R. Exploring the Benefits of B-Allyl Sulfones for More Homogeneous Dimethacrylate Photopolymer Networks. *Polym. Chem.* **2015**, *6*, 2038−2047.
(39) Lauger, J.; Linemann, R.; Richtering, W. Shear Orientation of a Lamellar Lyotropic Liquid-Crystal. *Rheol. Acta* **1995**, *34*, 132−136.
(40) Camerel, F.; Gabriel, J. C. P.; Batail, P.; Panine, P.; Davidson, P. Combined Saxs−Rheological Studies of Liquid-Crystalline Colloidal Dispersions of Mineral Particles. *Langmuir* **2003**, *19*, 10028−10035.
(41) Volker-Pop, L. M. Optical Methods in Rheology: Polarized Light Imaging. *Chem. Listy* **2014**, *108*, 707−710.
(42) Saarikoski, E.; Saarinen, T.; Salmela, J.; Seppala, J. Flocculated Flow of Microfibrillated Cellulose Water Suspensions: An Imaging Approach for Characterisation of Rheological Behaviour. *Cellulose* **2012**, *19*, 647−659.
(43) Bercea, M.; Navard, P. Shear Dynamics of Aqueous Suspensions of Cellulose Whiskers. *Macromolecules* **2000**, *33*, 6011−6016.
(44) Shafiei-Sabet, S.; Hamad, W. Y.; Hatzikiriakos, S. G. Rheology of Nanocrystalline Cellulose Aqueous Suspensions. *Langmuir* **2012**, *28*, 17124−33.
(45) Saarinen, T.; Haavisto, S.; Sorvari, A.; Salmela, J.; Seppala, J. The Effect of Wall Depletion on the Rheology of Microfibrillated Cellulose Water Suspensions by Optical Coherence Tomography. *Cellulose* **2014**, *21*, 1261−1275.
(46) Gleeson, J. T.; Larson, R. G.; Mead, D. W.; Kiss, G.; Cladis, P. E. Image-Analysis of Shear-Induced Textures in Liquid-Crystalline Polymers. *Liq. Cryst.* **1992**, *11*, 341−364.
(47) Mykhaylyk, O. O.; Warren, N. J.; Parnell, A. J.; Pfeifer, G.; Laeuger, J. Applications of Shear-Induced Polarized Light Imaging (Sipli) Technique for Mechano-Optical Rheology of Polymers and Soft Matter Materials. *J. Polym. Sci., Part B: Polym. Phys.* **2016**, *54*, 2151−2170.
(48) Hongladarom, K.; Secakusuma, V.; Burghardt, W. R. Relation between Molecular-Orientation and Rheology in Lyotropic Hydroxypropylcellulose Solutions. *J. Rheol.* **1994**, *38*, 1505−1523.
(49) Burghardt, W. R. Molecular Orientation and Rheology in Sheared Lyotropic Liquid Crystalline Polymers. *Macromol. Chem. Phys.* **1998**, *199*, 471−488.
(50) Lettinga, M. P.; Dogic, Z.; Wang, H.; Vermant, J. Flow Behavior of Colloidal Rodlike Viruses in the Nematic Phase. *Langmuir* **2005**, *21*, 8048−57.
(51) Larson, R. G.; Mead, D. W. Development of Orientation and Texture During Shearing of Liquid-Crystalline Polymers. *Liq. Cryst.* **1992**, *12*, 751−768.
(52) Ben Azouz, K.; Ramires, E. C.; Van den Fonteyne, W.; El Kissi, N.; Dufresne, A. Simple Method for the Melt Extrusion of a Cellulose Nanocrystal Reinforced Hydrophobic Polymer. *ACS Macro Lett.* **2012**, *1*, 236−240.
(53) Ranby, B. G. Aqueous Colloidal Solutions of Cellulose Micelles. *Acta Chem. Scand.* **1949**, *3*, 649−650.
(54) Gray, D. G.; Roman, M. Self-Assembly of Cellulose Nanocrystals: Parabolic Focal Conic Films. In *Cellulose Nanocomposites*; American Chemical Society, 2006; pp 26−32.
(55) Urena-Benavides, E. E.; Ao, G. Y.; Davis, V. A.; Kitchens, C. L. Rheology and Phase Behavior of Lyotropic Cellulose Nanocrystal Suspensions. *Macromolecules* **2011**, *44*, 8990−8998.

DOI: 10.1021/acsnano.8b02366
ACS Nano 2018, 12, 6926−6937

(56) Beck-Candanedo, S.; Roman, M.; Gray, D. G. Effect of Reaction Conditions on the Properties and Behavior of Wood Cellulose Nanocrystal Suspensions. *Biomacromolecules* **2005**, *6*, 1048–54.
(57) Liu, D. G.; Wang, S.; Ma, Z. S.; Tian, D. L.; Gu, M. Y.; Lin, F. Y. Structure-Color Mechanism of Iridescent Cellulose Nanocrystal Films. *RSC Adv.* **2014**, *4*, 39322–39331.
(58) Liu, D. G.; Chen, X. Y.; Yue, Y. Y.; Chen, M. D.; Wu, Q. L. Structure and Rheology of Nanocrystalline Cellulose. *Carbohydr. Polym.* **2011**, *84*, 316–322.
(59) Azzam, F.; Heux, L.; Jean, B. Adjustment of the Chiral Nematic Phase Properties of Cellulose Nanocrystals by Polymer Grafting. *Langmuir* **2016**, *32*, 4305–12.
(60) Liu, Q.; Smalyukh, I. I. Liquid Crystalline Cellulose-Based Nematogels. *Sci. Adv.* **2017**, *3*, e1700981.
(61) Gray, D. G. Chiral Nematic Ordering of Polysaccharides. *Carbohydr. Polym.* **1994**, *25*, 277–284.
(62) Parker, R. M.; Frka-Petesic, B.; Guidetti, G.; Kamita, G.; Consani, G.; Abell, C.; Vignolini, S. Hierarchical Self-Assembly of Cellulose Nanocrystals in a Confined Geometry. *ACS Nano* **2016**, *10*, 8443–8449.
(63) Barnes, H. A. The Yield Stress—a Review or 'Παντα Ρει'—Everything Flows? *J. Non-Newtonian Fluid Mech.* **1999**, *81*, 133–178.
(64) Qiao, C.; Chen, G.; Zhang, J.; Yao, J. Structure and Rheological Properties of Cellulose Nanocrystals Suspension. *Food Hydrocolloids* **2016**, *55*, 19–25.
(65) Araki, J.; Wada, M.; Kuga, S. Steric Stabilization of a Cellulose Microcrystal Suspension by Poly(Ethylene Glycol) Grafting. *Langmuir* **2001**, *17*, 21–27.
(66) Hirai, A.; Inui, O.; Horii, F.; Tsuji, M. Phase Separation Behavior in Aqueous Suspensions of Bacterial Cellulose Nanocrystals Prepared by Sulfuric Acid Treatment. *Langmuir* **2009**, *25*, 497–502.
(67) Zhou, Z. W.; Solomon, M. J.; Scales, P. J.; Boger, D. V. The Yield Stress of Concentrated Flocculated Suspensions of Size Distributed Particles. *J. Rheol.* **1999**, *43*, 651–671.
(68) Thomas, D. G. Transport Characteristics of Suspensions: Iii. Laminar-Flow Properties of Flocculated Suspensions. *AIChE J.* **1961**, *7*, 431–437.
(69) Studart, A. R.; Amstad, E.; Gauckler, L. J. Yielding of Weakly Attractive Nanoparticle Networks. *Soft Matter* **2011**, *7*, 6408–6412.
(70) Debord, S. B.; Lyon, L. A. Influence of Particle Volume Fraction on Packing in Responsive Hydrogel Colloidal Crystals. *J. Phys. Chem. B* **2003**, *107*, 2927–2932.
(71) Hao, T.; Riman, R. E. Calculation of Interparticle Spacing in Colloidal Systems. *J. Colloid Interface Sci.* **2006**, *297*, 374–7.
(72) Ureña-Benavides, E. E.; Kitchens, C. L. Wide-Angle X-Ray Diffraction of Cellulose Nanocrystal–Alginate Nanocomposite Fibers. *Macromolecules* **2011**, *44*, 3478–3484.
(73) Leppiniemi, J.; Lahtinen, P.; Paajanen, A.; Mahlberg, R.; Metsa-Kortelainen, S.; Pinomaa, T.; Pajari, H.; Vikholm-Lundin, I.; Pursula, P.; Hytonen, V. P. 3d-Printable Bioactivated Nanocellulose-Alginate Hydrogels. *ACS Appl. Mater. Interfaces* **2017**, *9*, 21959–21970.
(74) Mercader, C.; Lucas, A.; Derré, A.; Zakri, C.; Moisan, S.; Maugey, M.; Poulin, P. Kinetics of Fiber Solidification. *Proc. Natl. Acad. Sci. U. S. A.* **2010**, *107*, 18331–18335.
(75) Trebbin, M.; Steinhauser, D.; Perlich, J.; Buffet, A.; Roth, S. V.; Zimmermann, W.; Thiele, J.; Förster, S. Anisotropic Particles Align Perpendicular to the Flow Direction in Narrow Microchannels. *Proc. Natl. Acad. Sci. U. S. A.* **2013**, *110*, 6706–6711.
(76) Nesaei, S.; Rock, M.; Wang, Y.; Kessler, M. R.; Gozen, A. Additive Manufacturing with Conductive, Viscoelastic Polymer Composites: Direct-Ink-Writing of Electrolytic and Anodic Poly-(Ethylene Oxide) Composites. *Journal of Manufacturing Science and Engineering* **2017**, *139*, 111004–111004–12.
(77) Dunlop, J. W. C.; Fratzl, P. Biological Composites. *Annu. Rev. Mater. Res.* **2010**, *40*, 1–24.
(78) Fratzl, P.; Weinkamer, R. Nature's Hierarchical Materials. *Prog. Mater. Sci.* **2007**, *52*, 1263–1334.
(79) Reid, M. S.; Villalobos, M.; Cranston, E. D. Benchmarking Cellulose Nanocrystals: From the Laboratory to Industrial Production. *Langmuir* **2017**, *33*, 1583–1598.

DOI: 10.1021/acsnano.8b02366
ACS Nano 2018, 12, 6926–6937